Filling the gap of wind observations inside tropical cyclones

F. Tridon[1], A. Battaglia[1,2,3], A. Rizik[1], A. Illingworth[4]

[1]Dipartimento di Ingegneria dell'Ambiente, del Territorio, Politecnico di Torino, Turin, Italy
[2]Department of Physics and Astronomy, University of Leicester, Leicester, United Kingdom
[3]National Center for Earth Observation, Leicester, United Kingdom
[4]Department of Meteorology, University of Reading, Reading, United Kingdom

Key Points:

- Attenuation makes a spaceborne 94 GHz radar blind for only 5% of the cloudy/precipitating part of tropical cyclones
- Thanks to its scanning capability, WIVERN would provide 52 (40) times more observations of clouds (horizontal winds) than CloudSat in TCs
- Uncertainty in the winds measured by WIVERN will be dominated by the noise associated with Doppler radar measurements (around 3 m s^{-1} at 1 km)

Corresponding author: Frédéric Tridon, `frederic.tridon@polito.it`

Abstract

The WIVERN (WInd VElocity Radar Nephoscope) mission, currently under the Phase-0 of the ESA Earth Explorer program, promises to provide new insight in the coupling between winds and microphysics by globally observing, for the first time, vertical profiles of horizontal winds in cloudy areas. The objective of this work is to explore the potential of the WIVERN conically scanning Doppler 94 GHz radar for filling the wind observation gap inside tropical cyclones.

To this aim, realistic WIVERN notional observations of TCs are produced by combining the CloudSat 94 GHz radar reflectivity observations from 2007 to 2009 with ECMWF co-located winds. Despite the short wavelength of the radar (3 mm), which causes strong attenuation in presence of large amount of liquid hydrometeors, the system can profile most of the tropical cyclones, particularly the cloudy areas above the freezing level and the precipitating stratiform regions.

The statistical analysis of the results shows that, (i) because of its lower sensitivity, a nadir pointing WIVERN would detect 80% of the clouds (60% of winds with 3 m s^{-1} accuracy) observed by CloudSat, (ii) but thanks to its scanning capability, WIVERN would actually provide 52 times more observations of clouds (40 times more observations of horizontal winds) than CloudSat in TCs, (iii) this corresponds to more than 400 (300) million observations of clouds (accurate winds) every year. Such observations could be used in data assimilation models in order to improve numerical weather prediction and by modellers in order to shed light on the physical processes underpinning the evolution of tropical cyclones.

Plain Language Summary

Despite their huge impact on tropical weather, tropical cyclones are still not fully understood with limitations in the predictions of their evolution and trajectory. In order to provide more detailed observations of tropical cyclones, a ground-breaking spaceborne observing system hosting a conically scanning Doppler high frequency radar that could provide information both on in-cloud winds and cloud mass contents is proposed. Despite the fact that the observations from such radar are strongly attenuated in presence of heavy rain, the system can sample most of the tropical cyclones, particularly the cloudy areas above the freezing level and the precipitating stratiform regions. Our no-

tional study, based on the climatology of tropical cyclones collected during three years by a spaceborne non-Doppler radar, demonstrates that the newly proposed satellite would provide hundred millions observations of clouds and accurate winds in tropical cyclones every year. Such observations could be used to improve our understanding of the processes underpinning the evolution of tropical cyclones and hence, their forecast.

1 Introduction

Tropical cyclones (TCs) are probably the most iconic weather systems, for several reasons: they play a paramount role in the Earth's radiation budget and in the water cycle by transporting heat and moisture from the tropics to the mid-latitudes (Emanuel, 2001; Scoccimarro et al., 2011) and by releasing huge quantities of latent heat (Emanuel, 2003). But most importantly, they are among the most devastating of natural disasters causing widespread destruction due to strong wind and excessive amounts of rainfall when making landfall (Klotzbach et al., 2018).

There is still no widespread consensus on the understanding and prediction of the genesis of tropical cyclones (Emanuel, 2003). Several studies have found that environmental vertical wind shear (usually defined between 200 and 850 hPa) is the main driver for the formation, intensification, and dissipation of tropical cyclones because of its capability of causing kinematic and thermodynamic asymmetries (Thatcher & Pu, 2011; Schenkel et al., 2020; Wadler et al., 2022) but intertwined complex multiscale processes generally govern TC intensity change (Judt & Chen, 2016). The understanding of the dynamical and thermodynamical structure, of the cloud microphysics and its evolution during TC's life cycle is still a matter of active research and is crucial to improve forecasts (R. Rogers et al., 2013).

Another challenge with TCs is to predict their frequency and intensity response in a changing climate. This has been the subject of considerable investigation, often with conflicting results (Knutson et al., 2010; Emanuel, 2021). One of the factor explaining such inconsistencies is the differences in model physics (Walsh et al., 2016). Indeed, even with high resolution forecast models, biases in the physics were found to be responsible of a degradation of the forecasts of strong TCs when assimilating observations (Tong et al., 2018). To be confident in the predictions about the frequency of TCs in a future climate, it is important that the models are physically based and not empirically tuned.

Airborne radar observations have been used to understand mesoscale and convective-scale processes (e.g. convective bursts, downdrafts near the warm core, vortex Rossby waves, eyewall asymmetries) associated with the cyclone intensity change (R. F. Rogers et al., 2016; Guimond et al., 2020; Didlake et al., 2017; Wadler et al., 2018a). Observations and numerical experiments suggest the importance of wind observations for forecasting TC structure (J. E. George & Gray, 1976; Bucci et al., 2021) and the benefit of assimilating aircraft reconnaissance observations in improving TCs track and intensity forecasts (Tong et al., 2018). However, reconnaissance flight missions are scarce because they are primarily conducted for potentially landfalling storms. Progress is still hampered by the lack of high-resolution observations of the spatio-temporal evolution of the TC vertical structure of winds and clouds, especially over the oceans.

Satellite observations of winds can fill this gap. For example, recent studies have tested the impact of assimilating atmospheric motion vectors (AMVs) (Wu et al., 2014; C. Velden et al., 2017) or surface winds derived from ocean surface layer (Leidner et al., 2018; Cui et al., 2019). One limitation of such observations is that they are representative of a specific height, which can even be uncertain in the case of AMVs (C. S. Velden & Bedka, 2009; Cordoba et al., 2017). In 2018, the European Space Agency (ESA) launched the first spaceborne Doppler lidar (Aeolus) (Stoffelen et al., 2005) for measuring line-of-sight winds over an atmospheric column. This mission has been a fantastic success demonstrated by the operational follow-on mission called Aeolus-2 which will be launched within a decade (Wernham et al., 2021). It was shown that the assimilation of Aeolus observations generally improved forecasts of several numerical weather prediction models (NWP) (G. George et al., 2021; Rennie et al., 2021; Laroche & St-James, 2022). This includes positive impact in the forecast of TC intensity and size (Marinescu et al., 2022), despite Aeolus measurements being made in clear air and mostly coming from upper troposphere and lower stratosphere. However, it is well known that the tropospheric winds have a crucial role in steering TC tracks (J. E. George & Gray, 1976) and that assimilation of inner core — where most of the rain bands are present — winds is particularly useful for improving forecasts (Tong et al., 2018). Thus, because of the lack of penetration capability of lidar inside cloudy and rainy systems, this will remain an observation gap even in the Aeolus2 era.

The WIVERN (WInd VElocity Radar Nephoscope) mission (www.wivern.polito.it, (Illingworth et al., 2018; Battaglia, Martire, et al., 2022)), currently in Phase-0 within

the ESA Earth Explorer program, promises to complement the Aeolus measurements by globally observing, for the first time, vertical profiles of winds in cloudy and rainy areas by a conically scanning W-band (94 GHz) radar with polarization diversity capabilities. The objective of the mission is to extend the lead time of predictions of high-impact weather, including tropical cyclones and mid-latitude windstorms, and to improve short and medium-range weather forecasts by feeding, at a global scale, the Doppler measurements together with profiles of radar reflectivity and km-scale 94 GHz brightness temperatures into NWP models. It will provide global coverage about once a day with 500 m vertical and 10 km resolution resolution with an accuracy of 2 m s^{-1}. Such data can be assimilated into NWP models to improve the forecasting of the future track and intensity of TCs.

It is expected that the WIVERN 94 GHz radar will suffer from attenuation and multiple scattering effects in the presence of heavy rain and large amounts of ice contents (Protat et al., 2019; Matrosov et al., 2008; Battaglia et al., 2010). The scope of this paper is to assess the potential of the WIVERN mission to "see" inside tropical cyclones and provide simultaneous information about horizontal winds and cloud microphysics. In addition, the reduced WIVERN radar sensitivity compared to W-band non-scanning radars like the nadir-looking CloudSat and EarthCARE cloud profiling radars (Tanelli et al., 2008; Illingworth et al., 2015) will lower its cloud detection capabilities. Following Battaglia et al. (2018), this work exploits the multi-year CloudSat 94 GHz radar observations of tropical cyclones (Tourville et al., 2015) in combination with ECMWF reanalysis in order to simulate WIVERN-like W-band Doppler observations from a slant-looking radar (42° incidence angle).

Sect. 2 describes the methodology for simulating WIVERN observations starting from the CloudSat Tropical Cyclone Product; a statistical analysis on the expected performances from the radar is reported in Sect. 3, including the budget of wind measurements error in Sect. 3.4. Conclusions are drawn in Sect. 4.

2 Simulating WIVERN measurements from existing observations

2.1 CloudSat reflectivity curtains and ECMWF winds

The WIVERN radar is a 94 GHz conically scanning radar with a viewing angle of about 42° (see specifics in Tab. 1). As the antenna spins around at 12 rpm, it covers an

800-km wide swath and will make multiple observations of winds in every tropical cyclones about once a day (Illingworth et al., 2018). It will collect 2D curtains of reflectivity and Doppler velocities (Fabry, 2015) with 500 m vertical resolution inside the hurricane from all possible directions.

Table 1. Specifics currently envisaged for the polarization diversity Doppler radar of the WIVERN mission.

Spacecraft height, H_{sat}	500 km
Spacecraft velocity, v_{sat}	7600 m s^{-1}
Incidence angle, θ_i	41.6°
Radar frequency	94.05 GHz
Pulse length τ	3.3 μs
Antenna beamwidth, θ_{3dB}	0.071°
Antenna angular velocity, Ω_a	12 rpm
Footprint speed	500 km s^{-1}
Transmit polarization	H or V
Time separation between H and V pulses, T_{HV}	20 μs
Single pulse sensitivity	-15 dBZ
H-V Pair Repetition Frequency	4 kHz
Number of H-V Pairs per 1 km integration length	8

The best proxies for the WIVERN measurements are provided by the CloudSat CPR 94 GHz nadir-looking radar (Tanelli et al., 2009), together with winds from the ECMWF model. CloudSat has successfully collected data for more than 15 years and provided the first global observations of the cloud vertical structure of tropical cyclones. The ECMWF model winds are on the average unbiased (0.2 m s^{-1}) but statistical comparisons with Aeolus observations show that individual winds have a random error standard deviation of about 3 m s^{-1} (Rennie et al., 2021). A major limitation of the ECMWF winds is their coarse resolution which smooths out the variations. For example, Houchi et al. (2010) showed that the model can underestimate the wind shear by 10 times in comparison to high resolution radiosonde wind profiles. Hence, the ECWMF winds may not be fully representative of the actual wind shears.

Tourville et al. (2015) combined these two datasets leading to a collection of more than 10 million TC profiles of reflectivity and horizontal winds. Following the idea of Battaglia et al. (2018), WIVERN slant-looking reflectivity observations can be reconstructed from CloudSat nadir-looking radar observations of TCs and WIVERN Doppler velocities can be simulated from ECMWF winds.

2.2 Example of the typhoon Choi-Wan

The methodology is demonstrated in the case study of the typhoon Choi-Wan, a Category 5-equivalent super typhoon that developed over the Western Pacific in September 2009. Despite its intensity, no casualties were reported because its trajectory remained far from major inhabited land, only passing close to the Northern Mariana Islands. On September 11, 2009, a tropical depression formed 1,100 km to the east of Guam and rapidly intensified into a tropical cyclone. The intensification persisted through the following days until September 15, when Choi-Wan attained its peak intensity, with sustained winds peaking at 260 km h^{-1}. The typhoon remained very powerful until September 17 and weakened rapidly after September 19 to the East of Japan. Its high impact on ocean temperature, salinity and CO2 partial pressure was studied in Bond et al. (2011). On September 15, the A-train satellites made an overpass just north of the eye at the center of the storm, as shown by MODIS satellite visible observations (Fig. 1) and the CloudSat Cloud Profiling Radar reflectivity curtain (Fig. 2a).

Fig. 2 shows the CloudSat radar reflectivity observations (Fig. 2a), the cross-track ECMWF winds (Fig. 2b) and the cumulative two-way attenuation (Fig. 2c) derived from the CloudSat 2C-RAIN-PROFILE product (Haynes et al., 2009). The whole curtain is over the (Pacific) ocean as highlighted by the strong surface return. The radar reflectivity captures the vertical cross-section of the storm with its cloud structure. Most distinctive is the eye, which is completely clear down to sea level with thick clouds on either side of the eye towering in the inner eyewall region above fifteen kilometers. The transition between frozen and liquid precipitation is outlined by the radar bright band, which is consistently around the freezing level at 5 km height. Below the freezing level, liquid precipitation tends to attenuate the CPR signal, especially in the presence of moderate/heavy precipitation. In regions of strong attenuation where the surface return disappears (like for the profiles corresponding to the along-track distance between 1000 and 1200 km corresponding to the eye wall and the rain bands), the 2C-RAIN-PROFILE al-

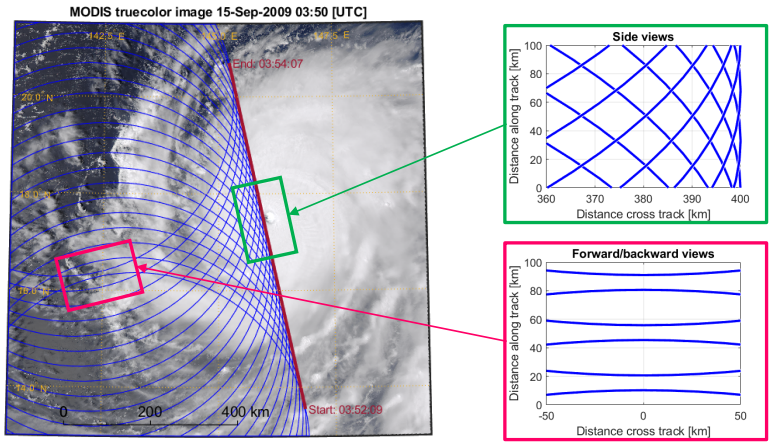

Figure 1. Visible image from the AQUA MODIS satellite of the Choi-Wan typhoon on September 15, 2009 between 03:51:38 and 03:54:37 with the CloudSat trajectory (red line) and the simulated scanning pattern of the conically scanning WIVERN radar as if it were observing the typhoon eye in side-view (blue line, 23 rotations, 115 s). The insets on the right show details of the region swept by the 3-dB footprints close to side views and to forward/backward views.

gorithm does not converge and the cumulative attenuation profile is retrieved down to 10 dB via the Hitschfeld and Bordan (1954) technique. All the segments of the profiles below such attenuation level (shaded region in Fig. 2a) are excluded from the WIVERN reconstruction since they are deemed to be adversely affected by vigorous convection and strong attenuation. Cross-track LOS winds are displayed in Fig. 2b. They roughly correspond to the zonal winds reduced by a factor $\sin\theta_i = 0.66$, with the typical inversion when going through the eye of the typhoon as expected from cyclonic circulation.

2.3 Simulation of WIVERN observations of the typhoon Choi-Wan

In Fig. 1, the 800-km wide ground track of the WIVERN antenna boresight is illustrated on top of the MODIS visible image of Choi-Wan for 23 rotations. Note that the scanning pattern of the radar footprints (an ellipse with minor and major axis equal to 0.75 and 1 km, respectively) will provide an 8% coverage of the swath with gaps of the order of 20 km between successive footprints behind the satellite track (forward/backward views inset in Fig. 1). On the contrary, there will be continuous coverage along the satellite direction at the swath edges (side view inset in Fig. 1). The CloudSat reflectivity

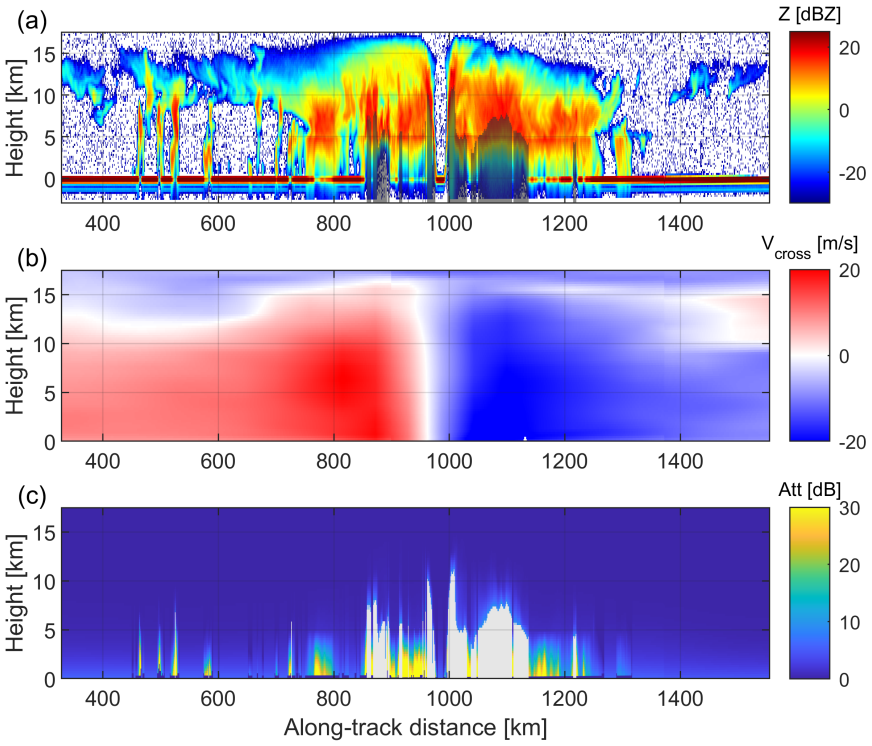

Figure 2. (a) CloudSat reflectivity curtain from the segment of granule 17996 corresponding to the overpass of the typhoon Choi-Wan on the 15 Sep 2009, (b) corresponding ECMWF wind in the direction across the CloudSat track (at 41°incidence angle), (c) path integrated attenuation retrieved by 2C-RAIN-PROFILE product or with the Hitschfeld and Bordan (1954) technique when the surface is not visible.

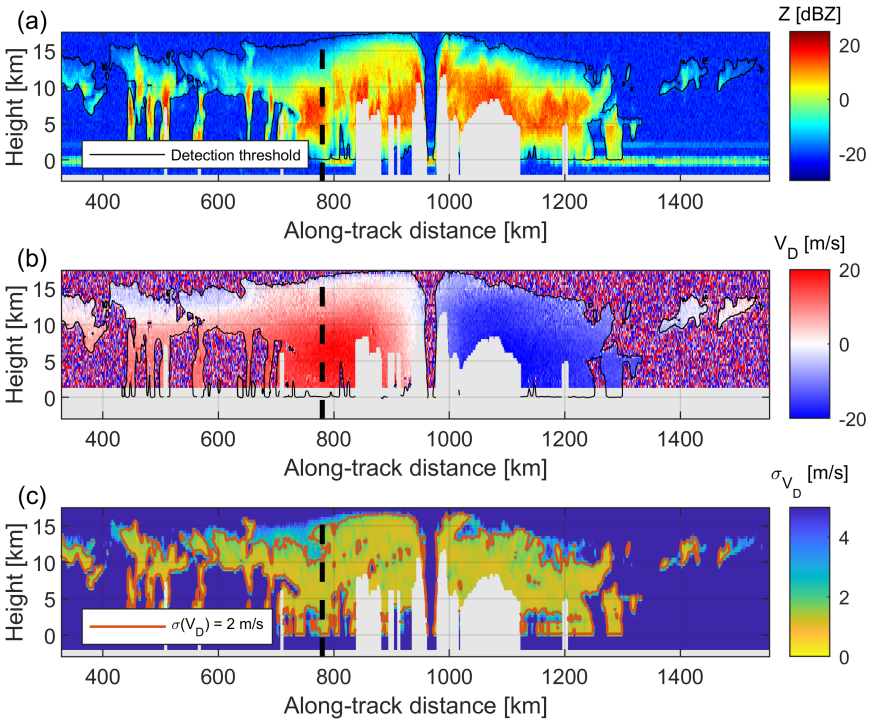

Figure 3. Simulated 1 km WIVERN (a) reflectivity curtain, (b) side-view Doppler velocity, and (c) expected Doppler velocity accuracy. The black dash vertical line indicates the position of the profile illustrated in Fig. 10.

curtain of Fig. 2a can be used for simulating the WIVERN observations in side view. This could indeed be the reconstructed curtain observed by WIVERN in the case its ground track was 400 km West of the CloudSat track, like in Fig. 1.

The WIVERN observations simulated in side view at 1 km integration are shown in Fig. 3. Most of the reflectivity features seen by the CloudSat radar are visible in WIVERN measurements. Because of the low number of independent pulses (8) and given its single pulse reflectivity equivalent noise floor at -15 dBZ, the WIVERN radar will have a slightly reduced sensitivity compared to CloudSat (e.g. some of the high clouds below -20 dBZ in Fig. 2 will not be detected by WIVERN). Like for CloudSat, strong attenuation will be encountered in the heavy precipitation parts below the freezing level; this is why such regions have been whitened. The surface returns are much weaker compared to the CloudSat observations, a clear advantage over CloudSat for sampling low precipitating clouds. This is due to the significant reduction in the normalized backscattering

cross sections of water surfaces when moving from nadir to 42° incidence angle (Battaglia et al., 2017).

According to the well established Doppler theory, the estimation of Doppler velocity improves with signal-to-noise ratio (SNR) and number of samples (i.e. with integration length). At high SNR, the WIVERN LOS Doppler velocities measurements are expected to come with a maximum accuracy of about 1.1 m s^{-1} at 1 km resolution and 0.4 m s^{-1} at 10 km resolution (see Sect. 3.4.1). Of course, the resulting mean wind accuracy cannot be as good and will depend on the SNR distribution of the observed clouds. Other sources of errors such as non-uniform beam filling and wind shear are discussed in Sect. 3.4. They have a lower impact on the wind precision, and the final accuracy of WIVERN measurements will be mainly driven by the Doppler estimation.

The LOS Doppler velocities depicted in Fig. 3b show increased noisiness when moving towards low signal-to-noise ratios (SNR). The accuracy of Doppler velocity shown in Fig. 3c takes into account the SNR of the reflectivity measurements. When SNR> 0 (i.e $Z > -15$dBZ), the measured velocity well reproduces the ECMWF fields with vast regions expected to have errors lower than 2 m s^{-1} (orange contour in Fig. 3c). On the contrary, when SNR$\ll 0$, the Doppler velocity measurements become random numbers within the Nyquist interval (-40 to +40 m s^{-1} for $T_{HV} = 20$ μs). In all the typhoon regions above the freezing level, the wind estimates have a reasonable accuracy, demonstrating the great potential of WIVERN observations in characterizing simultaneously the microphysical and dynamical structure of TCs at sub-freezing temperatures.

In order to improve cloud detection and wind accuracy, WIVERN observations can be averaged over a longer integration length. An example with a 10 km averaging distance is shown in Fig. 4. While Fig. 4 shows fewer details than Fig. 3, low reflective clouds are better detected (the area delimited by the detection threshold contour gets wider in Fig. 4a). Furthermore, the improved sensitivity leads to more accurate Doppler velocity measurements and the regions where errors lower than 2 m s^{-1} are expected are clearly more extended. While averaging along the track is generally considered useful for reducing the noise error, it can be detrimental when averaging over distances where reflectivity and winds are not uniform either because of intensity or direction, for example, regions with strong wind shears or in the proximity of convective cores. In order to eval-

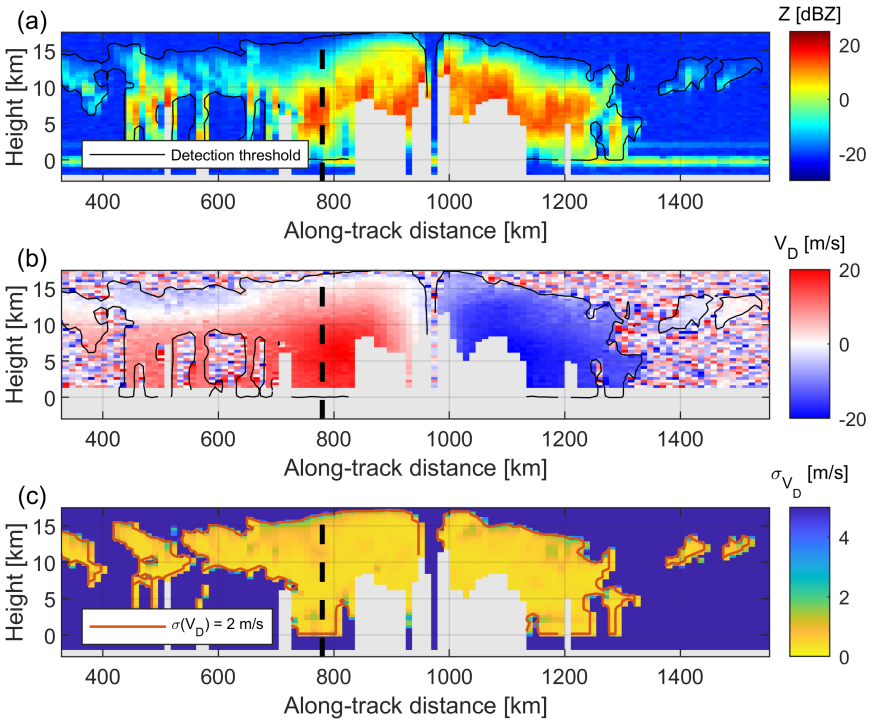

Figure 4. Same as Fig. 3 but with 10 km averaging distance.

uate the effect of averaging, several averaging distances have been used in the simulations and the respective results will be presented in sect. 3.

2.4 Detailed simulation procedure

The details about the simulation methodology are given in the appendix. In this section, we describe only the new features of the simulator which have been added in this study in comparison to Battaglia et al. (2018). Here, the non-uniform-beam-filling (NUBF) and wind shear (WS) effects are largely discussed because some of the new features allow to take them into account in a better way. However as noted above, these effects have a minor impact on Doppler velocity accuracy compared to the Doppler estimation (see discussion later in Sec. 3.4).

1. Instead of discarding entire CloudSat profiles where strong attenuation makes the ocean surface invisible and hence, prevents the application of the surface reference technique (Meneghini et al., 2000), an iterative attenuation correction (Hitschfeld

& Bordan, 1954) is applied down to the level where a 10 dB cumulative attenuation is reached. This preserves the original structure of the 2D reflectivity field and ensures realistic reflectivity gradients necessary for the correction of NUBF and WS effects.

2. The procedure described in the first item allows the inclusion of all surfaces and not only the ocean surfaces where a CloudSat path integrated estimate is possible via the surface reference technique (Meneghini et al., 2000). As a result, the entire CloudSat orbit can now be mapped into WIVERN observations.
3. In addition to the simulation of WIVERN observations in the forward direction, the option to simulate WIVERN observations in the side direction has been added. This allows to simulate the two extreme configurations where the satellite velocity has a maximum (forward) and minimum (side) contribution to NUBF error. In the forward view, the slant geometry of WIVERN is reconstructed from several successive CloudSat profiles, and the resulting vertical reflectivity gradients are used for NUBF and WS corrections. In the side view, the reflectivity is assumed to be horizontally homogeneous along the pointing direction, and the variability of the CloudSat reflectivity field allows to compute realistic horizontal gradients, which are the relevant gradients for the correction of NUBF error in this pointing direction. Another advantage of simulating WIVERN along the forward and side directions is that it provides more representative statistics of winds, with the forward view dominated by meridional winds and the side view dominated by zonal winds.

3 Statistical analysis

3.1 The CloudSat TC dataset

The CloudSat TC dataset includes CloudSat CPR intercepts of TCs within 1000 km of the storm center for the period between 2 Jun 2006 till 31 Dec 2013 for a total of 10.6 million radar profiles (more than 170,000 within 100 km) (Tourville et al., 2015). The years 2007, 2008 and 2009 have been analyzed, representing the core of the dataset with respectively 1244, 1411 and 1235 CloudSat overpasses (in comparison to the original dataset, we have excluded the overpasses where any of the CloudSat data product necessary for WIVERN simulation is missing, see Fig. A1) of 263 different tropical cyclones (with an average of 15 overpasses per cyclone). According to the overall statistics from Tourville

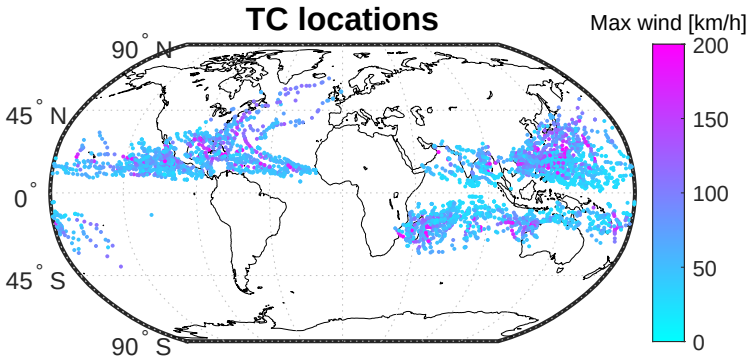

Figure 5. Location and max wind speed of all the tropical cyclones listed in the 2D-TC dataset for the year 2007.

et al. (2015), over the 2007-2009 period, CloudSat overpassed on average 4331 TCs with 5.8 million (93 thousand) radar profiles at 1 km integration along track within 1000 km (100 km) from TC center corresponding to an average of 1.9 million/year (31 thousand/year).

Fig. 5 shows the location and the maximum sustained 1-min wind speed of such storms as derived from the Automated Tropical Cyclone Forecasting System. The West Pacific basin region contains the greatest number of TC CPR intercepts (1143) followed by the Southern Hemisphere (1093), Atlantic (682), East Pacific (659), Indian Ocean (287) and Central Pacific (72) regions.

The contour frequency by altitude displays (CFAD) of the CloudSat reflectivity for the entire dataset (Fig. 6a) demonstrates that TC systems are typically very tall, they exhibit large reflectivities with highest values typically between 5 and 8 km, regions of sharp increase of reflectivities in the upper troposphere and regions of large attenuation below the freezing level (always at about 5 km) as highlighted by the sloping of reflectivities towards lower values in the lower troposphere.

Fig. 6b shows the CloudSat cloud types as function of height. Firstly, the total count of cloud peaks at about 0.4 million up to 14 km, meaning that about 20% of the pro-

files within 1000 km from TC center are cloudy. Secondly, the eight cloud class distribution demonstrates that in TC there is a mixture of cloud classes with a total of 32%, 9%, 5%, 4%, 7%, 21%, 22%, respectively for deep convection, nimbostratus, cumulus, stratocumulus, altocumulus, altostratus, and cirrus clouds. Therefore, though deep convection represents a large percentage of the entire cloud cover, the majority of clouds is likely to be found in areas where up and downdraft will not modify significantly the horizontal winds. These findings agree with previous research (Houze, 2010) that found a mixture of convective and stratiform precipitation (with the latter representing between 30 and 50% of the total) in the eyewall, inner core, and outer rainband region. In non-convective regions, WIVERN will be able to retrieve the horizontal LOS winds.

Finally, the CFADS of ECMWF horizontal winds projected in the LOS corresponding to the along and cross directions are shown in the bottom panels of Fig. 6. Winds show maximum amplitudes around 9-12 km but very seldom exceed 40 m s^{-1} (7‰ in the cross direction, and a factor 1000 less in the along direction). Therefore, biasing is not expected to be a serious issue in WIVERN measurement with $T_{HV} = 20$ μs, thus a Nyquist velocity of ± 40 m s^{-1}.

3.2 WIVERN cloud measurements in TC

The procedure described in the flowchart of Fig. A1 has been applied to the full 2007-2009 TC dataset. The first thing to establish is the impact of the slant-view and of the reduced sensitivity in the WIVERN capability in sensing clouds.

Even in intense precipitating systems such as tropical cyclones, the proportion of saturated profiles (where attenuation is so strong that attenuation correction of CloudSat reflectivity is not possible with good accuracy) is small in comparison to a large number of useful profiles. Fig. 7a demonstrates that only below 8 km some impact of attenuation (difference between the black and grey lines) is perceptible in CloudSat data. The lower sensitivity of WIVERN causes a reduction of the cloud detection at all levels and increasingly deteriorating when assuming worse single pulse sensitivities (compare magenta, blue, and green lines). Nevertheless, the cloud occurrence remains higher than 80% compared to the CloudSat reference for all levels between 2 and 10 km when adopting the baseline configuration of a single pulse sensitivity of -15 dBZ (Fig. 7b, green line) (thus a detection limit of about -20 dBZ when integrating 8 pulses in 1 km). The reduction

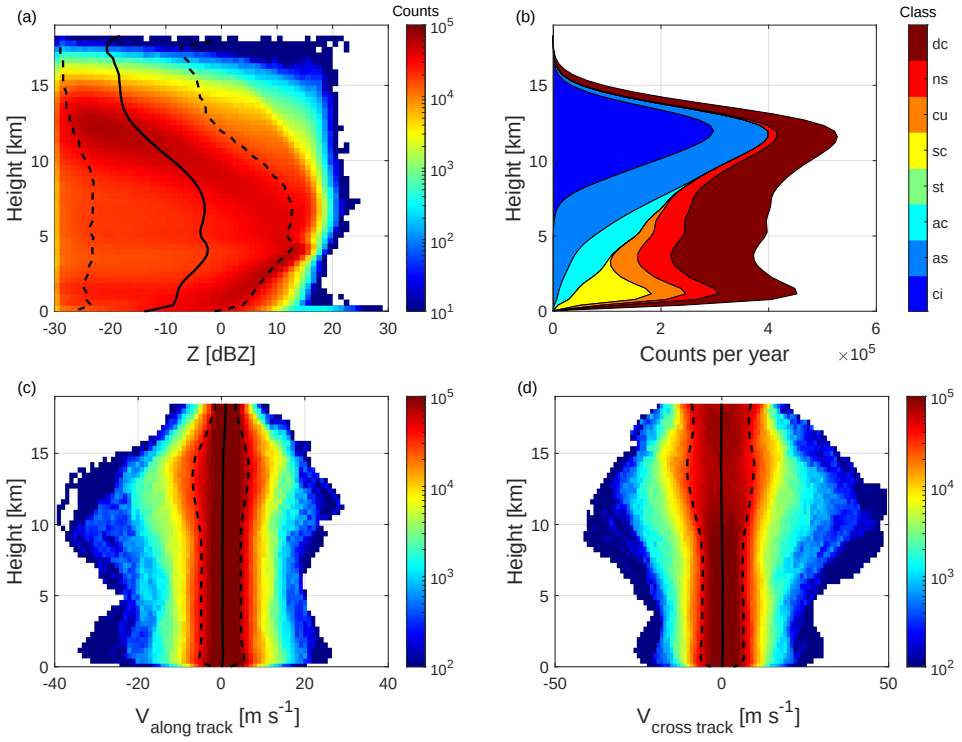

Figure 6. Top panels: reflectivity CFADS (a) and height cloud class distribution (b). DC: deep convection; NS: nimbostratus; CU: cumulus; SC: stratocumulus; ST: stratus; AC: altocumulus; AS: altostratus; CI: cirrus. Bottom panels: WIVERN LOS along-track (c) and cross-track winds (d).

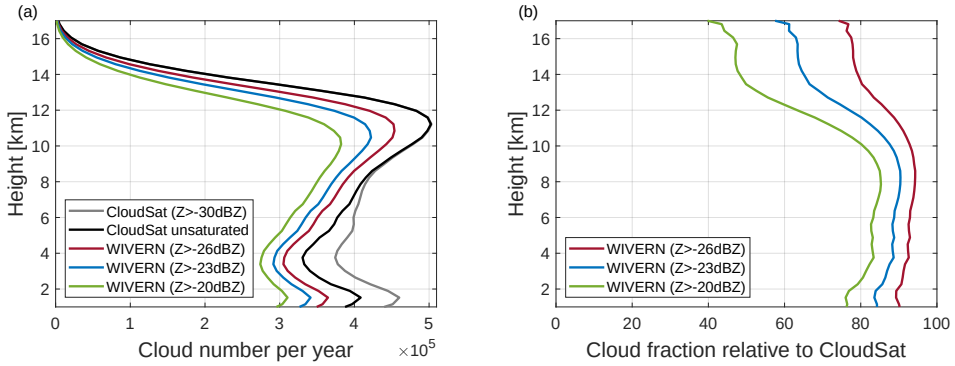

Figure 7. (a) Profiles of the annual number of clouds detected in TC by CloudSat or WIVERN with different detection limits as indicated in the legend. (b) Fraction of cloud detection relative to the CloudSat reference (black line in the left panel) for three different WIVERN detection limits.

in cloud detectability is limited to less than 10% compared to the CloudSat reference if the single pulse sensitivity (detection limit) is further improved toward -21 dBZ (-26 dBZ) (magenta line). Note that the CloudSat reference provides an average of about 0.4 million clouds at each level between 1 and 13 km in TC every year. Thanks to its fast conical rotation speed (footprint moving at about 500 km s^{-1}), WIVERN will sample weather features with a sampling rate 66 times larger than CloudSat (whose footprint moves at 7.6 km s^{-1}). Therefore, it will be 52 times more efficient than CloudSat for sampling tropical cyclones. Assuming layers of 650 m with a 20% cloud cover, we expect to detect about 400 million 1 km horizontally extended clouds in TC annually (exact computation from profiles of Fig. 7a and Fig. 7b leads to 447 million).

3.3 WIVERN wind measurements in TCs

The second step is to estimate how many winds better than a certain accuracy will be attainable from WIVERN measurements. Results are similar for forward and side pointing (only the results for forward pointing are shown in Fig. 8 for simplicity).

Realistic Doppler velocities that would be observed by WIVERN have been simulated for various sensitivities (20, -23, and -26 dBZ) and various integration lengths (1, 2 and 10 km). From the reflectivity and Doppler velocity gradients averaged over 1×5 km boxes, NUBF and WS errors corrections (Battaglia, Scarsi, et al., 2022) provide unbiased velocity estimates which are compared to the LOS wind velocity, finally yielding the wind residual statistics.

The occurrence of winds that would be measured with an accuracy better than 1 m s^{-1} (3 m s^{-1}) compared to the CloudSat cloud detection is shown in Fig. 8a (Fig. 8b). As can be expected, the probability of useful Doppler velocity estimates raises with an increasing sensitivity of the 94 GHz radar onboard WIVERN and a longer integration length. In particular, the integration length is greatly valuable for enhancing the number of highly precise Doppler velocity estimates (i.e. better than 1 m s^{-1}, Fig. 8a). When relaxing the required accuracy on the Doppler velocity (Fig. 8b), the benefit is less evident and the fraction of useful winds reach a maximum of about 75% for an accuracy better than 5 m s^{-1} (not shown).

Overall, the probability of precise Doppler velocity estimates (better than 3 m s^{-1}) will be more than 60% up to about 11 km height and will peak between 4 and 10 km

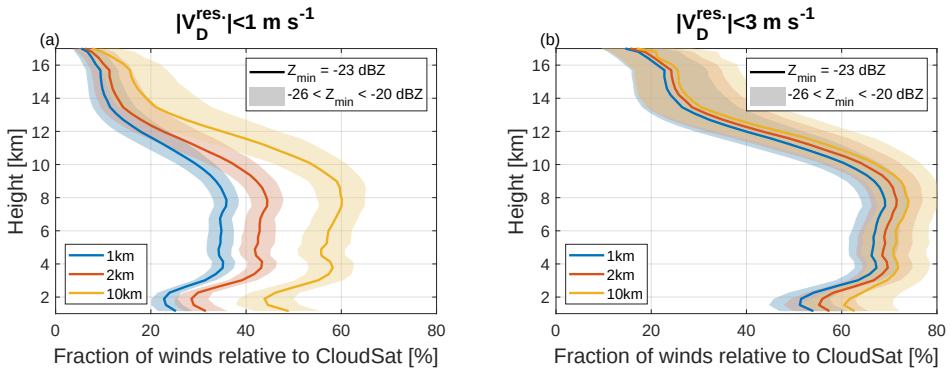

Figure 8. Profiles of the fraction of Doppler velocities as would be measured by WIVERN (relative to the CloudSat reference, black line in Fig. 7a) with an accuracy better than 1 (panel a) and 3 m s^{-1} (panel b) with averaging over 1 km, 2 and 10 km (see colors in legend) and different sensitivity levels.

height. Nevertheless, thanks to its 66 times better sampling, WIVERN would be 40 times more efficient than CloudSat if the latter were able to measure winds. Assuming layers of 650 m with a 20% cloud cover, this implies that WIVERN will measure about 300 million precise winds in Tropical Cyclones per year (the exact computation from profiles of Fig. 7a and 8b leads to 331 million).

3.4 Sources of error in WIVERN wind measurements

Different error sources can decrease the accuracy of WIVERN Doppler velocity. The advantage of running a simulator is that each error source can be evaluated separately. In the next sections, the different sources of errors are discussed and compared.

3.4.1 Errors associated with the polarization diversity pulse pair (PDPP) estimators

WIVERN reflectivities will be received in the two polarization channels. Cross-talk between the two channels will appear as low reflectivity ghosts 2.3 km above or below real targets (for example, ghosts arising from surface cross-talk are visible in Fig. 3a and 4a at around 2.3 km height as a horizontal line of low reflectivity standing out of the noise floor). While such ghosts will be generally easy to filter out in reflectivity measurements

(Rizik et al., n.d.), they will slightly increase the noise of the corresponding Doppler velocity, without introducing any bias.

In this configuration, the computation of WIVERN Doppler velocities will be done via the polarization diversity pulse pair technique (Battaglia, Martire, et al., 2022). Estimates of mean Doppler velocities from this technique are unbiased (apart when close to the Nyquist interval) and have an intrinsic noise associated with the phase and thermal noise (Pazmany et al., 1999). The precision of the Doppler measurements tends to improve with the correlation between the H and V pairs, the number of independent pulses that are averaged, higher levels of SNR (i.e. strong reflectivities), and signal to ghost ratio (SGR) (i.e. decreased contamination by ghosts). The standard deviation of the estimated Doppler velocity can be approximated as (Pazmany et al., 1999; Battaglia, Martire, et al., 2022):

$$\sigma_{\hat{v}_D}^{PDPP} = \frac{1}{\sqrt{2N}} \frac{v_{Nyq}}{\pi\beta} \sqrt{\left(1+\frac{1}{\mathrm{SNR}}\right)^2 + \frac{1}{\mathrm{SGR}_H} + \frac{1}{\mathrm{SGR}_V} + \frac{1}{\mathrm{SGR}_V \mathrm{SGR}_H} + \frac{1}{\mathrm{SNR}}\left(\frac{1}{\mathrm{SGR}_V} + \frac{1}{\mathrm{SGR}_H}\right) - \beta^2} \tag{1}$$

where:

$$\beta \equiv \rho_{HV}\, e^{-\frac{8\pi^2 \sigma_v^2 T_{HV}^2}{\lambda^2}} \qquad v_{Nyq} \equiv \frac{\lambda}{4T_{HV}}$$

where λ is the radar wavelength and σ_v is the spectral width of the Doppler spectrum. ρ_{HV} accounts for the decorrelation between the H and V pulses which is the result of intrinsic decorrelation associated to the hydrometeors (i.e. decorrelation at lag-0) and decorrelation due to the backscattering volume mismatch, i.e. to the fact that because of the antenna fast rotation, the two backscattering volumes for H and V pulses are not the same. The exponential term accounts for the time decorrelation due to the target reshuffling, which is proportional to λ/σ_v. Noise errors for a 5 km integration for different SNR levels are shown in Fig. 9. Monte Carlo simulations via I&Q (like done in Tanelli, Im, Facheris, and Smith (2002)) demonstrate that the approximated formula works satisfactorily at high SNRs and only slightly underestimates uncertainties at low SNRs (continuous vs. dashed lines).

3.4.2 Non-uniform beam filling and wind shear errors

Other sources of uncertainties are those due to reflectivity in-homogeneity within the backscattering volume and its coupling with the wind shear caused by the satellite

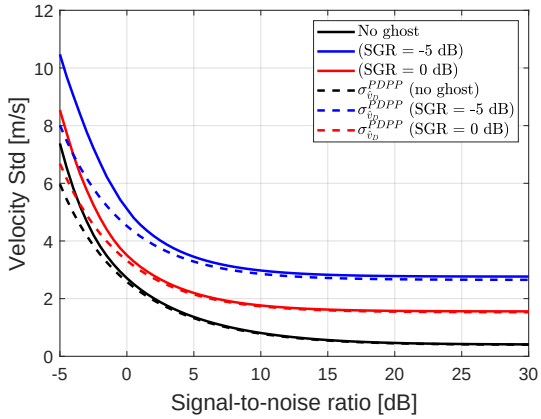

Figure 9. Doppler velocity standard deviation as a function of SNR for different signal-to-ghost ratios (SGR) at $T_{HV} = 20\,\mu$s and $\rho_{HV} = 1$ for a 5 km integration (corresponding to 40 H-V pulse pairs). Results computed using a Monte Carlo simulation of I&Qs (continuous lines) are compared with the analytical formula in Eq. (1 (dashed lines). Note that for the baseline configuration SNR= 0 dB corresponds to a reflectivity of -15 dBZ.

motion (named non-uniform beam filling bias (NUBF), Tanelli, Im, Durden, et al. (2002)) and with the atmospheric wind shear itself (hereafter named wind shear (WS) bias).

The mechanism for the generation of such errors is illustrated for a WIWERN forward-looking configuration in Fig. 10, in which a beam of twice 3-dB illuminates the scene in correspondence to the profile highlighted with a vertical dashed black line in Fig. 3. The corresponding NUBF and WS shear errors are shown in Fig. 11, together with the residual error in Doppler velocity after applying the corrections described below.

For a fast-moving spaceborne Doppler radar, radar reflectivity gradients within the radar sampling volume can introduce a significant source of error in Doppler velocity estimates, i.e. the NUBF errors (Tanelli, Im, Durden, et al., 2002). The Doppler velocity due to the satellite motion is first compensated for, according to the antenna boresight direction, and set to zero. Then the forward (backward) part of the backscattering volume appears to move upward (downward) as shown by the black contours in Fig. 10. Across the beam of twice 3-dB, this velocity ranges from -6 to +6 m s^{-1}. When coupled with a reflectivity gradient, this satellite-motion-induced velocity shear can produce a bias. For instance, in the portion of the profile above (below) 6 km, the tendency of the re-

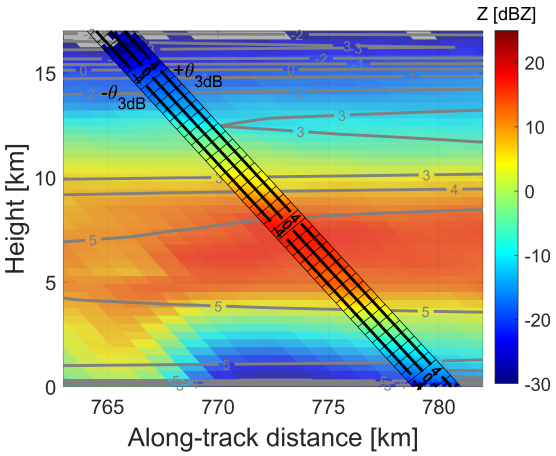

Figure 10. Illustration, in the forward direction configuration, of the sub-radar volume satellite-induced wind shear (as indicated by the black contour lines inside the antenna beam) and horizontal line-of-sight wind shear (values annotated in the gray contour lines) for the profile at 780 km (dashed black lines) in Fig. 3.

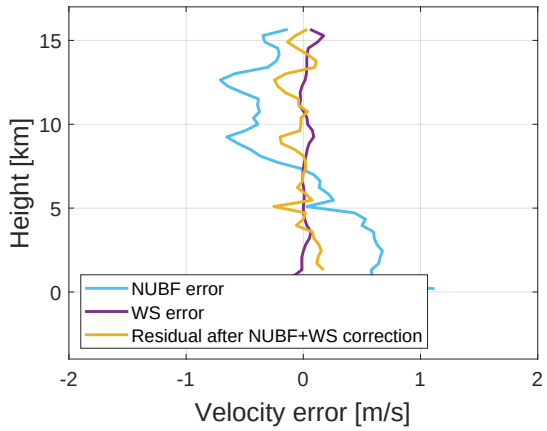

Figure 11. Demonstration of NUBF and WS bias corrections for the profile shown in Fig. 10.

flectivity to increase (decrease) towards the surface produces an upward (downward) bias (see blue line in Fig. 11).

The wind shear errors occur when reflectivity and velocity gradients are present at the same time within the backscattering volume. In the current profile, there are no strong wind shears (maximum of few m s^{-1} km^{-1}) and therefore WS errors never exceed ± 0.2 m s^{-1} (purple line in Fig. 11).

For nadir pointing radars, notional studies demonstrated that NUBF biases can be mitigated by estimating the along-track reflectivity gradient because NUBF-induced biases are, by definition, linearly proportional to such reflectivity gradients (Schutgens, 2008; Sy et al., 2014; Kollias et al., 2022). Similarly, in a slant-looking geometry, the relevant gradients are those along the direction orthogonal to the boresight and lying in the plane containing the satellite velocity and the antenna boresight direction (hereafter indicated as $\hat{\eta}$, Battaglia and Kollias (2015)). In a conically scanning system like WIVERN, it will be challenging to retrieve the Z-gradients along such directions and the correction will change according to the azimuthal scanning angle. For instance, when looking forward/backward, $\hat{\eta}$ is a combination of the vertical and of the horizontal along-track component, whereas when looking sideways, $\hat{\eta}$ coincides with the along-track direction.

For Gaussian circular antennas, if the reflectivity field can be approximated to vary linearly within the backscattering volume, then the bias introduced by the satellite motion is equal to (Sy et al., 2014; Battaglia & Kollias, 2015):

$$\Delta_{NUBF} = v_{sat}^{\perp BS} \frac{\nabla_{\hat{\eta}} Z}{4.343} \frac{1}{16\ \log(2)} r\theta_{3dB}^2 \tag{2}$$

where r is the range between the satellite and the ground along the boresight, and $v_{sat}^{\perp BS}$ is the ground-track satellite velocity orthogonal to the antenna boresight. The estimation of the reflectivity gradient along $\hat{\eta}$, $\nabla_{\hat{\eta}} Z$, is troublesome not only in the presence of noisy measurements but also because WIVERN will not sample reflectivities in all directions but will only produce a 2D slanted reflectivity curtain along the boresight track. Two extreme situations can be considered:

1. in side view, $\hat{\eta}$ coincides with the satellite trajectory so that $\nabla_{\hat{\eta}} Z$ can be properly estimated from the actual measurements and Eq. (2) can be used exactly with $v_{sat}^{\perp BS} = v_{sat}$;
2. in the forward and backward view, only the effect of the vertical gradient of reflectivities can be accounted for (which is likely the most relevant one, apart from when hitting cloud edges). Although the vertical gradients are not properly sampled by the slanted WIVERN geometry they can be well estimated because they are expected to be quite homogeneous on a scale of the order of a few kilometers. Eq. 2 then becomes:

$$\Delta_{NUBF}^{forward/backward} = v_{sat} \cos\theta_i \sin\theta_i \frac{\nabla_z Z}{4.343} \frac{r}{16\ \log(2)} \theta_{3dB}^2 \tag{3}$$

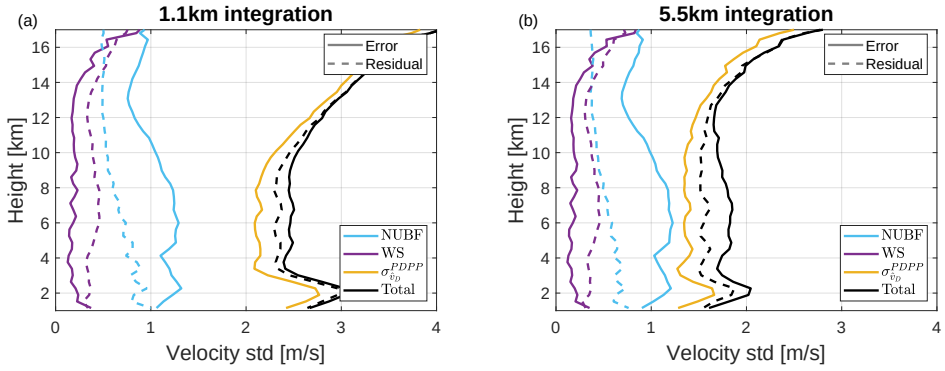

Figure 12. Profiles of the contribution from the main error sources (NUBF, WS, pulse pair estimator, see legend) on the Doppler velocity standard deviation at (a) 1 km and (b) 5 km integration. Dashed lines show the residual errors after the correction of NUBF and WS contribution as described in section 3.4.2

which for the WIVERN parameters corresponds to a bias of 0.077 m s^{-1} per dB km^{-1}.

3.4.3 Pointing errors

Any mispointing in the knowledge of the antenna boresight decreases the accuracy of the Doppler velocity because errors are introduced when subtracting the component of the satellite velocity parallel to the antenna boresight, $v_{sat}^{\|BS}$, along the antenna boresight. Different techniques to mitigate these errors are currently under study and are expected to contribute less than 0.3 m s^{-1} (Battaglia et al., n.d.)).

3.4.4 Error budget

The WIVERN simulator developed in this study allows to evaluate the contribution from each source of error separately. For instance, the satellite motion NUBF induced errors can be evaluated by computing the velocities running the simulator with or without satellite motion and then taking the differences between the two.

Using the TC dataset in forward view, the profiles of the relative contribution of pulse pair estimator, NUBF and WS are shown in Fig. 12 for 1 and 5 km integration lengths. At 1 km integration, the error from the pulse pair estimator is clearly the dominant term. It is maximum near cloud top where the SNR is low and is enhanced at around 2 km height where the surface's ghost generally degrades the accuracy of the wind. The next

contributor is the NUBF error and its correction is clearly efficient with a decrease of the error by a factor 1.5 in average. The correction of WS error on the other hand does not appear to be successful, but its contribution is anyway negligible compared to the two other terms. More work is needed to fully assess the performances of the NUBF and WS corrections using e.g. high resolution data from cloud resolving model outputs.

As expected when averaging over longer integration lengths, the apparent SNR increases and the pulse pair estimator error reduces substantially. Conversely, the contribution of NUBF and WS is only weakly effected by the noise level. For integration length larger than 10 km (not shown), the pulse pair estimator error starts to be dominated by the NUBF error and the correction of the latter becomes essential.

4 Summary and conclusions

The conically scanning Doppler W-band radar of the EE11 candidate WIVERN mission could provide for the first time global detailed observations of both the vertical structure of cloud and precipitation microphysics (including the location of convective cores) and, simultaneously, of the kinematic structure of the inner part of tropical cyclones (TCs).

Our study demonstrates that, despite the short wavelength of the radar (3 mm) which causes strong attenuation in presence of large amount of liquid hydrometeors, the system can profile most of the TCs, particularly the cloudy areas above the freezing level and the precipitating stratiform regions. Because of its lower sensitivity, the WIVERN radar would provide 80% observations of clouds and 60% accurate horizontal winds in TCs in comparison to CloudSat sampling, if it had the same sampling pattern. But thanks to its scanning antenna, WIVERN would actually provide 52 times more observations of clouds (and 40 times more observations of horizontal winds) than CloudSat. This will correspond to 447 million observations of clouds and 331 million observations of accurate winds every year inside TC, if WIVERN is launched.

At 1 km integration, the uncertainty of horizontal wind measurements will be dominated by the intrinsic noise associated with Doppler radar measurements and will be around 3 m s^{-1}. When averaging the measurements over longer integration lengths this uncertainty decreases to e.g. 1.5 m s^{-1} at 5 km integration. From 10 km integration, the error due to the wind shear caused by the satellite motion starts to be dominant and can

be corrected by about a half. Other sources of error such as averaging error cannot be addressed with the CloudSat data because ECMWF winds are defined over a too coarse resolution. They will be the focus of further studies based e.g. on cloud resolving model outputs.

Observations from WIVERN would complement the sparse observations from aircraft-reconnaissance measurements and by ground-based and airborne Doppler radars. These measurements should shed new light on the interaction between the inner TC core and the storm environment, e.g. thanks to a better understanding of the development of TC via the release of latent heat and the formation of precipitation.

It is also expected that the assimilation of these novel wind measurements will improve NWP's TC intensity forecasts already demonstrated for other microwaves active (Okamoto et al., 2016) and passive observations (Zhang et al., 2021; Duncan et al., 2022). Future work should assess the impact of the assimilation of TC WIVERN observations.

Appendix A Simulating WIVERN from CloudSat and ECMWF winds

The simulation methodology is sketched in Figure A1. As it was already described in details in Battaglia et al. (2018), only the main features are summarised below:

- First, the 94 GHz effective reflectivity, Z_{eff} (expressed in dBZ), and extinction coefficient, K_{ext} (expressed in dB m^{-1}), profiles are loaded from the 2C-RAIN-PROFILE (Haynes et al., 2009) product over ocean for the 2D CloudSat curtain. The derivation of the attenuation profile in the 2B-GEOPROF (Mace et al., 2007) product is based on the path integrated attenuation computed by the surface reference technique (Meneghini et al., 2000); this is only applicable over ocean without sea-ice. Over land, over sea-ice, and for strongly attenuated profiles over ocean, the profiles of extinction are partially reconstructed with the Hitschfeld and Bordan (1954) technique. The measured reflectivity Z_{co} (expressed in dBZ) at range r in the WIVERN slant geometry accounts for the increased cumulative attenuation compared to the nadir-looking view:

$$Z_{co}(r) = Z_{eff}(r) - 2\int_0^r K_{ext}(s)\, ds \tag{A1}$$

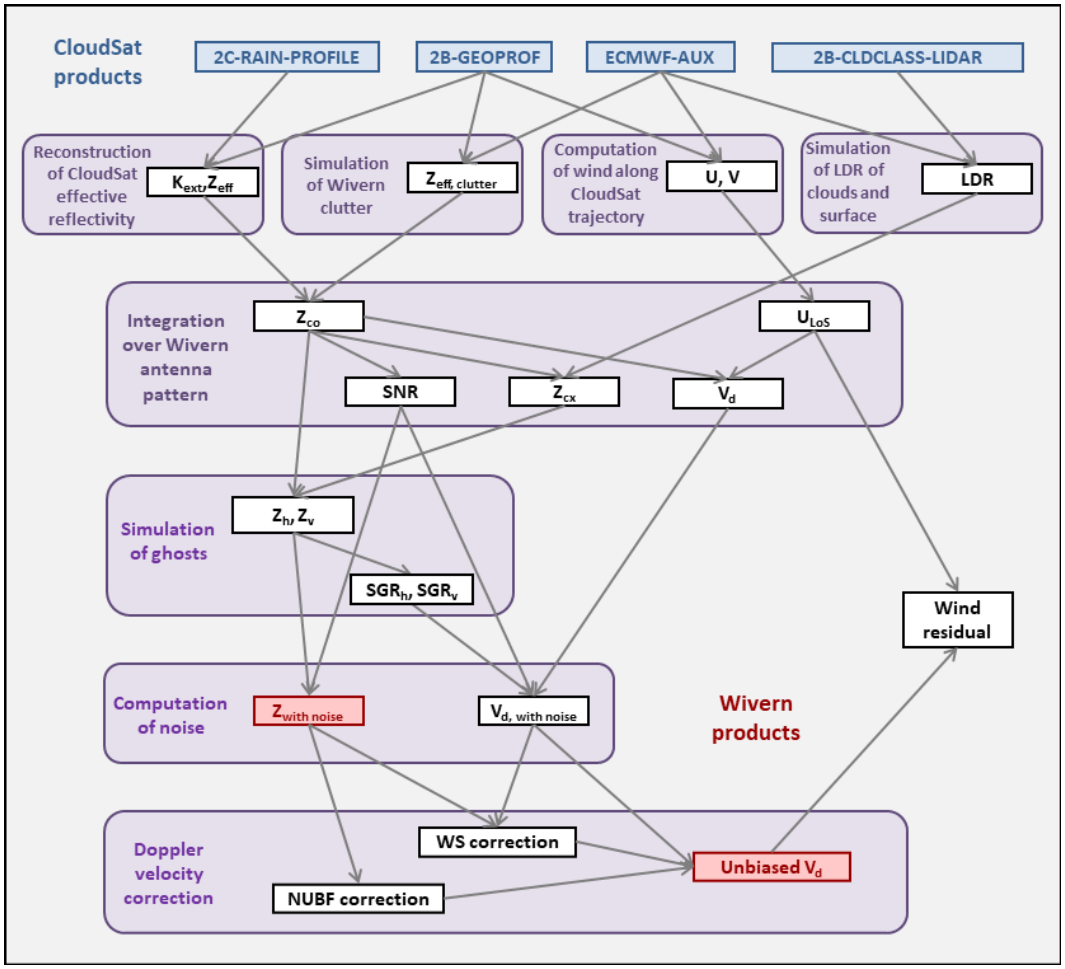

Figure A1. Flowchart describing the procedure to simulate WIVERN observations starting from CloudSat CPR observations and ECMWF reanalysis winds.

where the integral is carried out along the slant direction. The surface clutter position is derived from the 2B-GEOPROF product and modulated to the different WIVERN incidence angle according to airborne observations (Battaglia et al., 2017).

- Linear depolarization ratio (LDR, expressed in dB) values are reconstructed according to the temperature and the cloud type based on the 2B-CLDCLASS-LIDAR classification (Sassen et al., 2008): a climatology of the linear depolarization ratio profiles as function of temperature has been derived from data collected at the Chilbolton observatory during a specific field campaign when the W-band Galileo polarimetric radar was pointing at 45° elevation angle in June and July 2017. The resulting profiles of the 10^{th}, 25^{th}, 50^{th}, 75^{th} and 90^{th} percentiles are shown in Fig. A2. LDR values are reconstructed from the climatological quantiles assuming normal distributions with mean value and standard deviation depending on the cloud class and temperature range following Table A1. Since the LDR values are only needed for simulating the cross-talk effects, this approach is deemed sufficient for demonstrating the climatological impact of the ghosts on Doppler velocity accuracy. From profiles of Z_{co} and LDR, profiles of cross-polar reflectivities are computed as:

$$Z_{cx}(r) = Z_{co}(r) + \mathrm{LDR}(r). \tag{A2}$$

- Vertical profiles of line of sight (LOS) winds geo-located with CloudSat curtain are computed by projecting ECMWF horizontal winds from the ECMWF-AUX product onto the LOS; both along track and cross track winds are examined for simulating the "forward" and the "side" views.
- WIVERN reflectivities received in the two polarization channels, H and V, are simulated by taking into account the polarization diversity pulse-scheme (see Fig. 1 in Battaglia et al. (2013)). Intrinsic to such a scheme, there is cross-talk between the two channels (also referred to as ghosts) and separated in range by $\Delta r_{T_{HV}} = cT_{HV}/2$, T_{HV} being the separation between the two pulses:

$$Z_H[r] = Z_{co}[r] + Z_{cx}[r - \Delta r_{T_{HV}}] \tag{A3}$$

$$Z_V[r] = Z_{co}[r] + Z_{cx}[r + \Delta r_{T_{HV}}] \tag{A4}$$

the H being the polarization of the first pulse of the pair sequence.

- All quantities are integrated over the WIVERN antenna pattern and convolved with the point target response function to simulate the antenna weighted co-polar

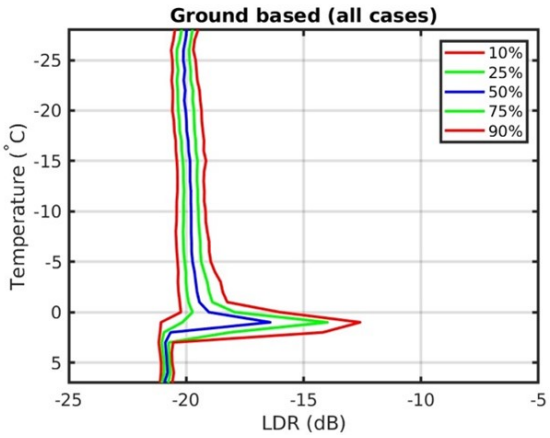

Figure A2. Dependence of LDR on temperature from radar observations at Chilbolton and corresponding ECMWF temperature profiles (courtesy of John Nicol, Weather Radar New Zealand).

reflectivity, $\langle Z_{co} \rangle_W$, the cross-polar reflectivity, $\langle Z_{cx} \rangle_W$ and the Doppler velocity, $\langle v_d \rangle_W$.

- Signal-to-ghost ratios (SGR) are computed as:

$$\mathrm{SGR}_H[r] \equiv \frac{\langle Z_{co}[r] \rangle_W}{\langle Z_{cx}[r - \Delta r_{T_{HV}}] \rangle_W} \tag{A5}$$

$$\mathrm{SGR}_V[r] \equiv \frac{\langle Z_{co}[r] \rangle_W}{\langle Z_{cx}[r + \Delta r_{T_{HV}}] \rangle_W} \tag{A6}$$

- Instrument noise and stochastic noise are added to the reflectivities and to the Doppler velocities according to the procedure described in Battaglia, Martire, et al. (2022). In order to evaluate the effect of the sensitivity of the WIVERN radar, different reflectivity equivalent noise levels at 1 km are used: -20, -23, and -26 dBZ.
- Doppler velocity corrections are implemented both for non-uniform beam filling (NUBF) and for wind shear (WS) according to the procedure described in Battaglia et al. (2018).

Data Availability Statement

The CloudSat tropical cyclone overpass data set is available at https://ade-laide.cira.colostate.edu/tc/ website.

Table A1. Mean value and standard deviation of LDR according to cloud class.

Cloud class	Temperature [$^{\circ}C$]	mean LDR [dB]	σ_{LDR} [dB]
ice	$T < -35$	-19	1.5
mixed	$-35 < T < -1$	-17	1.5
melting	$-1 < T < 4$	-14	1.5
rain	$T > 3$	-21	2

Acknowledgments

This research has been supported by the European Space Agency under the activities "WInd VElocity Radar Nephoscope (WIVERN) Phase 0 Science and Requirements Consolidation Study" (ESA Contract Number 4000136466/21/NL/LF) and "End-to-End Performance Simulator Activity of the WIVERN Mission" (ESA Contract Number 4000139446/22/NL/SD). This research used the Mafalda cluster at Politecnico di Torino.

References

Battaglia, A., Dhillon, R., & Illingworth, A. (2018). Doppler W-band polarization diversity space-borne radar simulator for wind studies. *Atm. Meas. Tech.*, *11*(11), 5965–5979. Retrieved from `https://www.atmos-meas-tech.net/11/5965/2018/` doi: 10.5194/amt-11-5965-2018

Battaglia, A., & Kollias, P. (2015). Error Analysis of a Conceptual Cloud Doppler Stereoradar with Polarization Diversity for Better Understanding Space Applications. *J. Atmos. Ocean Technol.*, *32*(7), 1298-1319. Retrieved from `https://doi.org/10.1175/JTECH-D-14-00015.1` doi: 10.1175/JTECH-D-14-00015.1

Battaglia, A., Martire, P., Caubet, E., Phalippou, L., Stesina, F., Kollias, P., & Illingworth, A. (2022). End to end simulator for the wivern w-band doppler conically scanning spaceborne radar. *Atm. Meas. Tech.*, *2021*, 1-31. Retrieved from `https://amt.copernicus.org/preprints/amt-2021-342/` doi: 10.5194/amt-2021-342

Battaglia, A., Scarsi, F., F., T., Dhillon, R., Martire, P., & Illingworth, A. (n.d.). Mispointing correction methods for the conically scanning wivern doppler

radar. *Atmospheric Measurement Techniques Discussion*. (in preparation)

Battaglia, A., Scarsi, F. E., Mroz, K., & Illingworth, A. (2022). Cross-calibration of millimeter conically scanning spaceborne radars. *Atm. Meas. Tech.*, *2022*, XXX. (in preparation)

Battaglia, A., Tanelli, S., Kobayashi, S., Zrnic, D., Hogan, R. J., & Simmer, C. (2010). Multiple-scattering in radar systems: A review. *J. Quant. Spectrosc. Radiat. Transfer*, *111*(6), 917 - 947. Retrieved from `http://www.sciencedirect.com/science/article/pii/S0022407309003677` doi: https://doi.org/10.1016/j.jqsrt.2009.11.024

Battaglia, A., Tanelli, S., & Kollias, P. (2013). Polarization Diversity for Millimeter Spaceborne Doppler Radars: An Answer for Observing Deep Convection? *J. Atmos. Ocean Technol.*, *30*(12), 2768-2787. Retrieved from `https://doi.org/10.1175/JTECH-D-13-00085.1` doi: 10.1175/JTECH-D-13-00085.1

Battaglia, A., Wolde, M., D'Adderio, L. P., Nguyen, C., Fois, F., Illingworth, A., & Midthassel, R. (2017). Characterization of Surface Radar Cross Sections at W-Band at Moderate Incidence Angles. *IEEE Trans. Geosci. Remote Sens.*, *55*(7), 3846-3859. (10.1109/TGRS.2017.2682423)

Bond, N. A., Cronin, M. F., Sabine, C., Kawai, Y., Ichikawa, H., Freitag, P., & Ronnholm, K. (2011). Upper ocean response to typhoon choi-wan as measured by the kuroshio extension observatory mooring. *Journal of Geophysical Research: Oceans*, *116*(C2). doi: https://doi.org/10.1029/2010JC006548

Bucci, L. R., Majumdar, S. J., Atlas, R., Emmitt, G. D., & Greco, S. (2021). Understanding the response of tropical cyclone structure to the assimilation of synthetic wind profiles. *Monthly Weather Review*, *149*(6), 2031 - 2047. doi: https://doi.org/10.1175/MWR-D-20-0153.1

Cordoba, M., Dance, S. L., Kelly, G. A., Nichols, N. K., & Waller, J. A. (2017). Diagnosing atmospheric motion vector observation errors for an operational high-resolution data assimilation system. *Quarterly Journal of the Royal Meteorological Society*, *143*(702), 333-341. doi: https://doi.org/10.1002/qj.2925

Cui, Z., Pu, Z., Tallapragada, V., Atlas, R., & Ruf, C. S. (2019). A preliminary impact study of cygnss ocean surface wind speeds on numerical simulations of hurricanes. *Geophysical Research Letters*, *46*(5), 2984-2992. doi: https://doi.org/10.1029/2019GL082236

Didlake, A. C., Heymsfield, G. M., Reasor, P. D., & Guimond, S. R. (2017). Concentric eyewall asymmetries in hurricane gonzalo (2014) observed by airborne radar. *Monthly Weather Review*, *145*(3), 729 - 749. Retrieved from `https://journals.ametsoc.org/view/journals/mwre/145/3/mwr-d-16-0175.1.xml` doi: https://doi.org/10.1175/MWR-D-16-0175.1

Duncan, D. I., Bormann, N., Geer, A. J., & Weston, P. (2022). Assimilation of amsu-a in all-sky conditions. *Monthly Weather Review*, *150*(5), 1023 - 1041. Retrieved from `https://journals.ametsoc.org/view/journals/mwre/150/5/MWR-D-21-0273.1.xml` doi: https://doi.org/10.1175/MWR-D-21-0273.1

Emanuel, K. (2001). Contribution of tropical cyclones to meridional heat transport by the oceans. *Journal of Geophysical Research: Atmospheres*, *106*(D14), 14771-14781. doi: https://doi.org/10.1029/2000JD900641

Emanuel, K. (2003). Tropical cyclones. *Annual Review of Earth and Planetary Sciences*, *31*(1), 75-104. doi: 10.1146/annurev.earth.31.100901.141259

Emanuel, K. (2021). Response of global tropical cyclone activity to increasing co2: Results from downscaling cmip6 models. *Journal of Climate*, *34*(1), 57 - 70. doi: https://doi.org/10.1175/JCLI-D-20-0367.1

Fabry, F. (2015). *Radar Meteorology: Principles and Practice*. Cambridge University Press. doi: 10.1017/CBO9781107707405

George, G., Halloran, G., Kumar, S., Rani, S. I., Bushair, M., Jangid, B. P., ... Maycock, A. (2021). Impact of aeolus horizontal line of sight wind observations in a global nwp system. *Atmospheric Research*, *261*, 105742. Retrieved from `https://www.sciencedirect.com/science/article/pii/S0169809521002982` doi: https://doi.org/10.1016/j.atmosres.2021.105742

George, J. E., & Gray, W. M. (1976). Tropical cyclone motion and surrounding parameter relationships. *Journal of Applied Meteorology and Climatology*, *15*(12). doi: https://doi.org/10.1175/1520-0450(1976)015⟨1252:TCMASP⟩2.0.CO;2

Guimond, S. R., Reasor, P. D., Heymsfield, G. M., & McLinden, M. M. (2020). The dynamics of vortex rossby waves and secondary eyewall development in hurricane matthew (2016): New insights from radar measurements. *J. Atmos. Sci.*, *77*(7), 2349 - 2374. Retrieved from `https://journals.ametsoc.org/view/journals/atsc/77/7/jasD190284.xml` doi: https://doi.org/10.1175/JAS-D-19-0284.1

Haynes, J. M., L'Ecuyer, T. S., Stephens, G. L., Miller, S. D., Mitrescu, C., Wood, N. B., & Tanelli, S. (2009). Rainfall retrieval over the ocean with spaceborne W-band radar. *J. Geophys. Res. Atm.*, *114*(D8). Retrieved from https://agupubs.onlinelibrary.wiley.com/doi/abs/10.1029/2008JD009973 doi: 10.1029/2008JD009973

Hitschfeld, W., & Bordan, J. (1954). Errors inherent in the radar measurement of rainfall at attenuating wavelengths. *J. Meteor.*, *11*, 58-67.

Houchi, K., Stoffelen, A., Marseille, G. J., & Kloe, J. D. (2010). Comparison of wind and wind shear climatologies derived from high-resolution radiosondes and the ECMWF model. *J. Geophys. Res.*, *115*(D22123). (doi:10.1029/2009JD013196)

Houze, R. A. (2010). Clouds in tropical cyclones. *Monthly Weather Review*, *138*(2), 293 - 344. Retrieved from https://journals.ametsoc.org/view/journals/mwre/138/2/2009mwr2989.1.xml doi: https://doi.org/10.1175/2009MWR2989.1

Illingworth, A. J., Barker, H. W., Beljaars, A., Ceccaldi, M., Chepfer, H., Clerbaux, N., ... van Zadelhoff, G.-J. (2015). The EarthCARE Satellite: The Next Step Forward in Global Measurements of Clouds, Aerosols, Precipitation, and Radiation. *Bull. Amer. Met. Soc.*, *96*(8), 1311-1332. Retrieved from https://doi.org/10.1175/BAMS-D-12-00227.1 doi: 10.1175/BAMS-D-12-00227.1

Illingworth, A. J., Battaglia, A., Bradford, J., Forsythe, M., Joe, P., Kollias, P., ... Wolde, M. (2018). WIVERN: A New Satellite Concept to Provide Global In-Cloud Winds, Precipitation, and Cloud Properties. *Bull. Amer. Met. Soc.*, *99*(8), 1669-1687. Retrieved from https://doi.org/10.1175/BAMS-D-16-0047.1 doi: 10.1175/BAMS-D-16-0047.1

Judt, F., & Chen, S. S. (2016). Predictability and dynamics of tropical cyclone rapid intensification deduced from high-resolution stochastic ensembles. *Monthly Weather Review*, *144*, 4395–4420.

Klotzbach, P. J., Bowen, S. G., Pielke, R., & Bell, M. (2018). Continental u.s. hurricane landfall frequency and associated damage: Observations and future risks. *Bull. Amer. Met. Soc.*, *99*(7), 1359 - 1376. Retrieved from https://journals.ametsoc.org/view/journals/bams/99/7/bams-d-17-0184.1.xml doi: https://doi.org/10.1175/BAMS-D-17-0184.1

Knutson, T. R., McBride, J. L., Chan, J., Emanuel, K., Holland, G., Landsea, C., ... Sugi, M. (2010, March). Tropical cyclones and climate change. *Nature Geoscience*, *3*(3), 157-163. doi: 10.1038/ngeo779

Kollias, P., Puidgomènech Treserras, B., Battaglia, A., Borque, P., & Tatarevic, A. (2022). Processing reflectivity and doppler velocity from earthcare's cloud profiling radar: the c-fmr, c-cd and c-apc products. *EGUsphere*, *2022*, 1–25. Retrieved from https://egusphere.copernicus.org/preprints/2022/egusphere-2022-1284/ doi: 10.5194/egusphere-2022-1284

Laroche, S., & St-James, J. (2022). Impact of the aeolus level-2b horizontal line-of-sight winds in the environment and climate change canada global forecast system. *Quarterly Journal of the Royal Meteorological Society*, *148*(745), 2047-2062. doi: https://doi.org/10.1002/qj.4300

Leidner, S. M., Annane, B., McNoldy, B., Hoffman, R., & Atlas, R. (2018). Variational analysis of simulated ocean surface winds from the cyclone global navigation satellite system (cygnss) and evaluation using a regional osse. *Journal of Atmospheric and Oceanic Technology*, *35*(8), 1571 - 1584. doi: https://doi.org/10.1175/JTECH-D-17-0136.1

Mace, G. G., Marchand, R., Zhang, Q., & Stephens, G. (2007). Global hydrometeor occurrence as observed by CloudSat: Initial observations from summer 2006. *Geophys. Res. Lett.*, *34, L09808*. (doi:10.1029/2006GL029017)

Marinescu, P. J., Cucurull, L., Apodaca, K., Bucci, L., & Genkova, I. (2022). The characterization and impact of aeolus wind profile observations in noaa's regional tropical cyclone model (hwrf). *Quarterly Journal of the Royal Meteorological Society*, *148*(749), 3491-3508. doi: https://doi.org/10.1002/qj.4370

Matrosov, S. Y., Battaglia, A., & Rodriguez, P. (2008). Effects of Multiple Scattering on Attenuation-Based Retrievals of Stratiform Rainfall from CloudSat. *J. Atmos. Ocean Technol.*, *25*(12), 2199-2208. Retrieved from https://doi.org/10.1175/2008JTECHA1095.1 doi: 10.1175/2008JTECHA1095.1

Meneghini, R., Iguchi, T., Kozu, T., Liao, L., Okamoto, K., Jones, J. A., & Kwiatkowski, J. (2000). Use of the Surface Reference Technique for Path Attenuation Estimates from the TRMM Precipitation Radar. *J. Appl. Meteorol.*, *39*(12), 2053-2070. Retrieved from https://doi.org/10.1175/1520-0450(2001)040<2053:UOTSRT>2.0.CO;2 doi: 10.1175/

700 1520-0450(2001)040⟨2053:UOTSRT⟩2.0.CO;2

701 Okamoto, K., Aonashi, K., Kubota, T., & Tashima, T. (2016). Experimental assim-
702 ilation of the gpm core observatory dpr reflectivity profiles for typhoon halong
703 (2014). *Monthly Weather Review*, *144*(6), 2307-2326. Retrieved from `https://`
704 `doi.org/10.1175/MWR-D-15-0399.1` doi: 10.1175/MWR-D-15-0399.1

705 Pazmany, A. L., Galloway, J. C., Mead, J. B., Popstefanija, I., McIntosh, R. E.,
706 & Bluestein, H. W. (1999). Polarization Diversity Pulse-Pair Technique
707 for Millimeter-WaveDoppler Radar Measurements of Severe Storm Fea-
708 tures. *J. Atmos. Ocean Technol.*, *16*(12), 1900-1911. Retrieved from
709 `https://doi.org/10.1175/1520-0426(1999)016<1900:PDPPTF>2.0.CO;2`
710 doi: 10.1175/1520-0426(1999)016⟨1900:PDPPTF⟩2.0.CO;2

711 Protat, A., Rauniyar, S., Delanoë, J., Fontaine, E., & Schwarzenboeck, A. (2019).
712 W-Band (95 GHz) Radar Attenuation in Tropical Stratiform Ice Anvils. *J.*
713 *Atmos. Ocean Technol.*, *36*(8), 1463-1476. Retrieved from `https://doi.org/`
714 `10.1175/JTECH-D-18-0154.1` doi: 10.1175/JTECH-D-18-0154.1

715 Rennie, M. P., Isaksen, L., Weiler, F., de Kloe, J., Kanitz, T., & Reitebuch, O.
716 (2021). The impact of aeolus wind retrievals on ecmwf global weather fore-
717 casts. *Quarterly Journal of the Royal Meteorological Society*, *147*(740), 3555-
718 3586. doi: https://doi.org/10.1002/qj.4142

719 Rizik, A., Battaglia, A., Tridon, F., Scarsi, F., Kötsche, A., Kalesse-Los, H., ...
720 Illingworth, A. (n.d.). Impact of cross-talk on reflectivity and doppler measure-
721 ments for the wivern polarization diversity doppler radar. *IEEE Trans. Geosci.*
722 *Remote Sens.*.

723 Rogers, R., Reasor, P., & Lorsolo, S. (2013). Airborne doppler observations of
724 the inner-core structural differences between intensifying and steady-state
725 tropical cyclones. *Monthly Weather Review*, *141*(9), 2970 - 2991. Re-
726 trieved from `https://journals.ametsoc.org/view/journals/mwre/141/`
727 `9/mwr-d-12-00357.1.xml` doi: https://doi.org/10.1175/MWR-D-12-00357.1

728 Rogers, R. F., Zhang, J. A., Zawislak, J., Jiang, H., Alvey, G. R., Zipser, E. J.,
729 & Stevenson, S. N. (2016). Observations of the structure and evolution of
730 hurricane edouard (2014) during intensity change. part ii: Kinematic struc-
731 ture and the distribution of deep convection. *Monthly Weather Review*,
732 *144*(9), 3355 - 3376. Retrieved from `https://journals.ametsoc.org/view/`

journals/mwre/144/9/mwr-d-16-0017.1.xml doi: https://doi.org/10.1175/MWR-D-16-0017.1

Sassen, K., Wang, Z., & Liu, D. (2008). The global distribution of cirrus clouds from CloudSat/CALIPSO measurements. *Geophys. Res. Lett.*, *113*(D00A12). (doi:10.1029/2008JD009972)

Schenkel, B. A., Edwards, R., & Coniglio, M. (2020). A climatological analysis of ambient deep-tropospheric vertical wind shear impacts upon tornadoes in tropical cyclones. *Weather and Forecasting*, *35*(5), 2033 - 2059. Retrieved from https://journals.ametsoc.org/view/journals/wefo/35/5/wafD190220.xml doi: https://doi.org/10.1175/WAF-D-19-0220.1

Schutgens, N. A. J. (2008). Simulated Doppler Radar Observations of Inhomogeneous Clouds: Application to the EarthCARE Space Mission. *J. Atmos. Ocean Technol.*, *25*(9), 1514-1528. (doi: 10.1175/2007JTECHA1026.1)

Scoccimarro, E., Gualdi, S., Bellucci, A., Sanna, A., Fogli, P. G., Manzini, E., ... Navarra, A. (2011). Effects of tropical cyclones on ocean heat transport in a high-resolution coupled general circulation model. *Journal of Climate*, *24*(16), 4368 - 4384. Retrieved from https://journals.ametsoc.org/view/journals/clim/24/16/2011jcli4104.1.xml doi: https://doi.org/10.1175/2011JCLI4104.1

Stoffelen, A., Pailleux, J., Kallen, E., Vaughan, J. M., Isaksen, L., Flamant, P., ... Ingmann, P. (2005). The Atmospheric Dynamics Mission for Global Wind Field Measurement. *Bull. Amer. Met. Soc.*, *86*, 73-87.

Sy, O. O., Tanelli, S., Takahashi, N., Ohno, Y., Horie, H., & Kollias, P. (2014, Feb). Simulation of EarthCARE Spaceborne Doppler Radar Products Using Ground-Based and Airborne Data: Effects of Aliasing and Nonuniform Beam-Filling. *IEEE Trans. Geosci. Remote Sens.*, *52*(2), 1463-1479. doi: 10.1109/TGRS.2013.2251639

Tanelli, S., Durden, S. L., Im, E., Heymsfield, G., Racette, P., & Starr, D. (2009). Next-generation spaceborne cloud profiling radars. In IEEE (Ed.), *Radar conference* (p. 1-4). (10.1109/RADAR.2009.4977116)

Tanelli, S., Durden, S. L., Im, E., Pak, K. S., Reinke, D. G., Partain, P., ... Marchand, R. T. (2008, Nov). CloudSat's Cloud Profiling Radar After Two Years in Orbit: Performance, Calibration, and Processing. *IEEE Trans. Geosci. Remote*

Sens., *46*(11), 3560-3573. doi: 10.1109/TGRS.2008.2002030

Tanelli, S., Im, E., Durden, S. L., Facheris, L., & Giuli, D. (2002). The Effects of Nonuniform Beam Filling on Vertical Rainfall Velocity Measurements with a Spaceborne Doppler Radar. *J. Atmos. Ocean Technol.*, *19*(7), 1019-1034. Retrieved from `https://doi.org/10.1175/1520-0426(2002)019<1019:TEONBF>2.0.CO;2` doi: 10.1175/1520-0426(2002)019⟨1019:TEONBF⟩2.0.CO;2

Tanelli, S., Im, E., Facheris, L., & Smith, E. A. (2002). DFT-based spectral moment estimators for spaceborne Doppler precipitation radar. In *Proc. of symp. on rem. sens. of the atmosphere, environment and space (spie 4894-50).* Hangzhou (RPC).

Thatcher, L., & Pu, Z. (2011). How vertical wind shear affects tropical cyclone intensity change: An overview. In A. Lupo (Ed.), *Recent hurricane research* (chap. 13). Rijeka: IntechOpen. Retrieved from `https://doi.org/10.5772/15416` doi: 10.5772/15416

Tong, M., Sippel, J. A., Tallapragada, V., Liu, E., Kieu, C., Kwon, I.-H., ... Zhang, B. (2018). Impact of assimilating aircraft reconnaissance observations on tropical cyclone initialization and prediction using operational hwrf and gsi ensemble–variational hybrid data assimilation. *Monthly Weather Review*, *146*(12). doi: https://doi.org/10.1175/MWR-D-17-0380.1

Tourville, N., Stephens, G., DeMaria, M., & Vane, D. (2015). Remote sensing of tropical cyclones: Observations from cloudsat and a-train profilers. *Bull. Amer. Met. Soc.*, *96*(4), 609 - 622. Retrieved from `https://journals.ametsoc.org/view/journals/bams/96/4/bams-d-13-00282.1.xml` doi: https://doi.org/10.1175/BAMS-D-13-00282.1

Velden, C., Lewis, W. E., Bresky, W., Stettner, D., Daniels, J., & Wanzong, S. (2017). Assimilation of high-resolution satellite-derived atmospheric motion vectors: Impact on hwrf forecasts of tropical cyclone track and intensity. *Monthly Weather Review*, *145*(3), 1107 - 1125. doi: https://doi.org/10.1175/MWR-D-16-0229.1

Velden, C. S., & Bedka, K. M. (2009). Identifying the uncertainty in determining satellite-derived atmospheric motion vector height attribution. *Journal of Applied Meteorology and Climatology*, *48*(3), 450 - 463. doi: https://doi.org/10.1175/2008JAMC1957.1

Wadler, J. B., Cione, J. J., Zhang, J. A., Kalina, E. A., & Kaplan, J. (2022). The effects of environmental wind shear direction on tropical cyclone boundary layer thermodynamics and intensity change from multiple observational datasets. *Monthly Weather Review*, *150*(1), 115 - 134. Retrieved from `https://journals.ametsoc.org/view/journals/mwre/150/1/MWR-D-21-0022.1.xml` doi: https://doi.org/10.1175/MWR-D-21-0022.1

Wadler, J. B., Rogers, R. F., & Reasor, P. D. (2018a). The relationship between spatial variations in the structure of convective bursts and tropical cyclone intensification as determined by airborne doppler radar. *Monthly Weather Review*, *146*, 761–780.

Walsh, K. J., McBride, J. L., Klotzbach, P. J., Balachandran, S., Camargo, S. J., Holland, G., ... Sugi, M. (2016). Tropical cyclones and climate change. *WIREs Climate Change*, *7*(1), 65-89. doi: https://doi.org/10.1002/wcc.371

Wernham, D., Heliere, A., Mason, G., & Straume, A. G. (2021). Aeolus-2 mission pre-development status. In *2021 ieee international geoscience and remote sensing symposium igarss* (p. 767-770). doi: 10.1109/IGARSS47720.2021.9554716

Wu, T.-C., Liu, H., Majumdar, S. J., Velden, C. S., & Anderson, J. L. (2014). Influence of assimilating satellite-derived atmospheric motion vector observations on numerical analyses and forecasts of tropical cyclone track and intensity. *Monthly Weather Review*, *142*(1), 49 - 71. doi: https://doi.org/10.1175/MWR-D-13-00023.1

Zhang, Y., Sieron, S. B., Lu, Y., Chen, X., Nystrom, R. G., Minamide, M., ... Zhang, F. (2021). Ensemble-based assimilation of satellite all-sky microwave radiances improves intensity and rainfall predictions for hurricane harvey (2017). *Geophys. Res. Lett.*, *48*(24), e2021GL096410. Retrieved from `https://agupubs.onlinelibrary.wiley.com/doi/abs/10.1029/2021GL096410` (e2021GL096410 2021GL096410) doi: https://doi.org/10.1029/2021GL096410